SOOT FORMATION AND CARBON MONOXIDE PRODUCTION IN BUOYANCY-DRIVEN PARALLEL VERTICAL WALL FIRE - A COMPUTER STUDY

H.Y. Wang
Institut Pprime (CNRS-UPR 3346), Département Fluide-Thermique-Combustion, ENSMA - BP 40109
Téléport 2, 1 av Clément ADER, F-86961 Futuroscope Chasseneuil Cedex, France

(Received 9 February 2009; Accepted 29 January 2013)

ABSTRACT

This study concerns the modelling of buoyancy-dominated turbulent diffusion flames including the CO production and the soot formation in parallel vertical burning walls geometry. Controlling mechanisms of three dimensional flow, combustion via a two-step reaction scheme, soot production and radiation are coupled with a Large Eddy Simulation (LES) approach. An eddy-dissipation concept accounts for the interaction between combustion, soot and turbulence. The numerical models are first validated using experimental data from the vertical wall fires, and later used for a parametric study by varying the separation distance (L) between the burning walls and the pyrolysis rate, m_F. The level of the CO production appears less sensitive to the change in the ratio, L/H, between the spacing (L) and height (H), and however, the ratio, L/H, has a significantly pronounced impact on the soot formation. Of particular interest is a minimum in soot formation for a ratio, L/H, of 0.2 due to the enough oxygen and the stronger interaction between the two diffusion flames in the merging region, both enhancing the soot oxidation. In the case where a merging of the diffusion flames occurs (L/H < 0.2), a critical pyrolysis rate of 10 g/m^{2}s is predicted, beyond which the combustion efficiency enters rapidly the decay phase up to about 60%. As the pyrolysis rate surpasses this critical value, the flame height, H_f, past the burning wall is approximately two times of the burning wall height ($H_f \approx 2H$). Globally, change in the pyrolysis rate has a more pronounced impact on the amplitude of both the soot and CO productions than variation in the ratio, L/H.

1. INTRODUCTION

The majority of all fires that have occurred in the industry, and particularly in storage arrays in warehouse, is rather serious due to a strong flames interaction in parallel configuration. A naturally induced air flow moving upward along a vertical channel between adjacent stacks leads to a fast flame spread over surface of a condensed fuel. Up to now, a large number of numerical, experimental or empirical studies are carried out only over a free vertical burning surface. For numerical simulation, this simplified configuration allows the use of a parabolic calculation scheme by assuming that the separation distance between the walls is infinitely great. To the best knowledge of the authors, the first numerical and experimental analyses addressing a parallel wall fire, as shown in Fig. 1, are the works of Tamanini [1], in which a parabolic scheme was extended to simulate such configuration by preassigning a free-parallel stream velocity. Flame radiation is found to be a dominant factor affecting the burning rate. While the convective heat transfer has been thought to play an important role in controlling the rate of downward laminar flame spread along vertical parallel sheets of thin combustible solid [2]. Further works [3-4] on turbulent flames have suggested that changes in the heat fluxes at walls in vertical parallel configurations are induced by a change in the dominant heat flux mechanism from radiation to convection as the separation is reduced. The recent works [5-6] concentrated on the radiation flux in a parallel vertical panel geometry, and the fire is supplied by a sand burner at the base of the panels.

Fig. 1: Instantaneous view of the burning between parallel vertical walls from a video camera

In most fires, carbon monoxide and smoke (soot) from products of incomplete combustion represent the principal life threat. A set of comprehensive experiment [7-9] for a jet flame or an enclosure fire is included for determining the yields of CO and soot, defined as the fraction of the fuel mass that is converted into CO and soot as a function of the global equivalence ratio. As the combustion is controlled by the local mixing processes between oxygen and fuel, the work of Hyde and Moss [10] describes CO production in terms of the mixture fraction for a given vitiated environment. A mixture fraction combustion model is used in the Fire Dynamics Simulator (FDS) code [11], in which soot and CO production are described from a correlation [7] for well-ventilated fires. In the work of Peters [12], the turbulent combustion model incorporates a two-step reaction scheme together with an eddy-dissipation concept by using k-ε turbulence model, to formulate interaction between combustion and turbulence. It is found that the carbon monoxide fired from an industrial-scale, natural gas burner has been predicted with a good accuracy. Up to now, no single CFD code can incorporate all of the physical and chemical processes that are of importance for under-ventilated vertical channel fires. This consideration has provided the main motivation for the present work, to use a combustion model via a two-step reaction scheme [12], in addition to a soot formation model [13] for addressing the important issue of CO and soot production. Several authors [14-15] have shown the limit of the use of Reynolds Averaged Navier-Stokes (RANS) k-ε turbulence model to simulate the highly oscillating buoyancy-induced turbulent vertical diffusion flame. Thus, Large Eddy Simulation (LES) for the fluid dynamic equations of three-dimensional elliptic, reacting flow is chosen by coupling with soot and radiation models. The numerical models are verified by checking only the mean temperature and velocity profiles against experimental measurements from both a wall fire in parallel configuration [3] and a free vertical burning surface [14]. The research presented provides fundamental numerical knowledge on the effects of pyrolysis rate and separation distance between the burning walls on soot and CO production, and heat transfer in parallel configuration with a buoyancy-induced air flow.

2. THEORETICAL ANALYSIS

Implementations of a combustion model via two sequential, semi-global steps, and a soot formation model within Large Eddy Simulation (LES) for the fluid dynamic equations are described briefly in this section.

2.1 Fluid Dynamic Equations

LES is based on a filtering operation, which decomposes a full flowfield, $\phi(x,t)$, into a resolved component, $\bar{\phi}(x,t)$, and a SubGrid-Scale (SGS) component, $\phi'(x,t)$. Here, $\phi(x,t)$ stands for a generic fluid property which represents the dependent variables, such as the velocity, u_i/u_j, the pressure, p, the enthalpy, h, and the mass fraction, Y_i. Applying the filtering operation to each term in the conservation equations of mass, momentum, energy and species, and decomposing the dependent variables into resolved and subgrid components results in the filtered governing equations, shown below :

$$\frac{\partial \rho}{\partial t} + \frac{\partial \rho \bar{u}_j}{\partial x_j} = 0 \tag{1}$$

$$\frac{\partial \rho \bar{u}_i}{\partial t} + \frac{\partial (\rho \bar{u}_i \bar{u}_j)}{\partial x_j} + \frac{\partial \bar{p}}{\partial x_i} - \rho g_i = \nabla \cdot \bar{\tau}_{ij,SGS} \tag{2}$$

where an overbar denotes the filtered variable, ρ the density, and t the time. The symbols, x_i and x_j, represent the co-ordinate system, and g_i the acceleration of gravity in the co-ordinate directions. The unresolved field, $\phi'(x,t)$, is modelled by the Smagorinsky model [16] in which the SGS Reynolds stresses tensor, $\bar{\tau}_{ij,SGS}$, are related to the local large scale rate of strain, $\bar{S}_{ij}$.

$$\bar{\tau}_{ij,SGS} = 2\mu_t \bar{S}_{ij} \text{ and } \bar{S}_{ij} = \frac{1}{2}\left(\frac{\partial \bar{u}_i}{\partial x_j} + \frac{\partial \bar{u}_j}{\partial x_i} \right) \tag{3}$$

Following the analysis of Smagorinsky [16], the eddy viscosity, μ_t, can be modelled as,

$$\mu_t = C_s^2 \rho \Delta^2 \left| \bar{S}_{ij} \right| \tag{4}$$

Here, $\left|\bar{S}_{ij}\right|$ is the magnitude of the large scale strain rate tensor, $\bar{S}_{ij}$, $\Delta = (\Delta x \Delta y \Delta z)^{1/3}$ the filter width, and C_s an empirical constant with an experimentally-determined value of 0.21. The turbulent heat flux is based on an eddy viscosity assumption, resulting in the following equation for the enthalpy, h :

$$\frac{\partial \rho \bar{h}}{\partial t} + \frac{\partial (\rho \bar{u}_i \bar{h})}{\partial x_j} - \frac{\partial}{\partial x_j}\left(\frac{\mu_t}{Pr_t} \frac{\partial \bar{h}}{\partial x_j} \right) = \dot{q}_c''' - \nabla \cdot q_r \tag{5}$$

where Pr_t denotes the turbulent Prandtl number with a usually used value of 0.5. The energy equation includes the rate of heat release per unit

volume, $\dot{q}_c'''$, and the radiant energy flux, $-\nabla \cdot q_r$. Finally, the perfect gas law is used to describe the equation of state.

2.2 Combustion Model

The combustion model is based on a chemical reaction, which is proceed via two sequential, semi-global steps to CO prediction [12]. It is assumed that a hydrocarbon, C_xH_y, oxidizes to carbon monoxide, CO, and water, H_2O, while intermediate CO oxidizes to CO_2 :

$$1\,kg\_C_xH_y + \nu_1^* kg\_O_2 \rightarrow \frac{28}{12} f_c\ kg\_CO + \frac{18}{2}(1-f_c)\,kg\_H_2O \tag{6}$$

$$1\,kg\_CO + \nu_2\ kg\_O_2 \rightarrow (1+\nu_2)\,kg\_CO_2 \tag{7}$$

Here, ν_1^* and ν_2 denote the stoichiometric coefficients, defined as follows :

$$\nu_1^* = \nu_1 - \frac{28}{12} f_c \nu_2 \ ; \ \nu_1 = \frac{32}{12} f_c + \frac{16}{2}(1-f_c) \ ; \ \nu_2 = \frac{16}{28} \tag{8}$$

The carbon fraction in C_xH_y is denoted by f_c. The combustion processes are governed by the conservation equations similar to Eq.(5) for the mass fraction, Y_i, of the six major chemical species (i=C_xH_y, O_2, CO, CO_2, H_2O and N_2). It should be noted that, in most fires, the chemistry determining heat release is fast in comparison with the key timescales which characterise turbulent mixing and the latter is therefore rate controlling. However, it is not currently applicable for the computational tools to distinguish the respective rates of mixing-controlled reaction, such as the chemistry of particulate soot formation or CO production. The combustion processes are crudely accounted for by Eddy Break-Up (EBU) concept, without introducing an unacceptably large computational overhead. In this approach, the local reaction rate, $\dot{\omega}_{CxHy}$, for fuel and $\dot{\omega}_{CO}$, for carbon monoxide is calculated as,

$$\dot{\omega}_{CxHy} = \frac{d\rho Y_{CxHy}}{dt} = -\rho \tau_{mix} \min(Y_{CxHy}, \frac{Y_{O2}}{\nu_1^*}) \tag{9}$$

$$\dot{\omega}_{CO} = \frac{d\rho Y_{CO}}{dt} = -\rho \tau_{mix} \min(Y_{CO}, \frac{Y_{O2}}{\nu_2}) \tag{10}$$

In most fires, the primary momentum transport and turbulent diffusion are sustained by large-scale energy-containing eddies, and the key timescales, τ_{mix} , are related approximately to the resolved dissipation rate.

$$\tau_{mix} \approx C_{Ebu} \frac{\varepsilon}{k} \tag{11}$$

where C_{Ebu} is an empirical constant in EBU approach with a standard value of 4. In the parlance of the turbulence community, the turbulent kinetic energy, k, is related to the eddy viscosity, μ_t, by the relation

$$k = \left(\frac{\mu_t}{C_\mu \rho \Delta} \right)^2 \tag{12}$$

and its dissipation, ε , can be derived from the turbulent kinetic energy as,

$$\varepsilon = C_\varepsilon \frac{k^{3/2}}{\Delta} \tag{13}$$

Here, Δ is a length scale, and C_μ , C_ε are the turbulent constants, given as 0.0856 and 0.845, respectively. In the case of the two combustibles burning, the CO production rate, S_{CO}, and required oxygen consumption rate, $\dot{\omega}_{O2}$, read respectively,

$$S_{CO} = \dot{\omega}_{CO} - \frac{28}{12} f_c \dot{\omega}_{CxHy} \ ; \quad \dot{\omega}_{O2} = \nu_1^* \omega_{CxHy} + \nu_2 \dot{\omega}_{CO} \tag{14}$$

The heat release rate, $\dot{q}_c$, is directly proportional to the rate of consumption of oxygen [17].

$$\dot{q}_c = -H_o \dot{\omega}_{O2} \tag{15}$$

Here, H_o is the amount of energy released per unit mass of oxygen consumed with a value of 13100 kJ/kg. This model allows for taking into account the progressive vitiation of the ambient medium during a confined fire growth.

2.3 Soot Formation and Its Oxidation

In a heavily sooting flame, soot particles generated from combustion processes have a significant impact on the radiative heat transfer characteristics. Various detailed soot formation models [18] would require accurate knowledge of fuel composition (C_2H_2, C_6H_5, C_6H_6, OH, etc). However, coupling between LES and the detail chemistry to track the soot development stages in relation to its formation and destruction is not available due to the prohibitive computation cost for large-scale fire simulation. In this work, the soot formation and its oxidation are incorporated into a turbulent flow calculation in two convection-diffusion equations for the filtered soot number density, n, and soot volume fraction, f_v, expressed as follows,

$$\frac{\partial \rho \bar{n}}{\partial t} + \frac{\partial}{\partial x_j}\left[\rho(\bar{u}_i + \bar{u}_i^{th})\bar{n}\right] - \frac{\partial}{\partial x_j}\left(\frac{\mu_t}{Sc_t}\frac{\partial \bar{n}}{\partial x_j}\right) = \dot{\omega}_n - \bar{n}\,\dot{\omega}_{Oxid} \tag{16}$$

$$\frac{\partial \rho \bar{f}_v}{\partial t} + \frac{\partial}{\partial x_j}\left[\rho(\bar{u}_i + u_i^{th})\bar{f}_v\right] - \frac{\partial}{\partial x_j}\left(\frac{\mu_t}{Sc_t}\frac{\partial \bar{f}_v}{\partial x_j}\right) = \dot{\omega}_{fv} - \bar{f}_v\,\dot{\omega}_{Oxid} \tag{17}$$

Here, u_i^{th} is the mean thermophoretic velocity components :

$$u_i^{th} = -0.54\nu\frac{\partial \ln \bar{T}}{\partial x_i} \tag{18}$$

Here, ν denotes the cinematic viscosity. A recent soot model that incorporates the essential physical process of soot nucleation, coagulation and surface growth is developed principally by Moss et al. [13] since soot production is described simply in terms of the local temperature, T, and the mole fraction of fuel gas, X_{CxHy}. The local formation rate, $\dot{\omega}_n$, for the soot number density, and $\dot{\omega}_{fv}$, for the soot volume fraction is calculated as,

$$\dot{\omega}_n = C_\alpha N_0 \rho^2 \bar{T}^{1/2} \bar{X}_{CxHy} e^{-T_\alpha/\bar{T}} - \frac{C_\beta}{N_0}\bar{T}^{1/2}\bar{n}^2 \tag{19}$$

$$\dot{\omega}_{fv} = \frac{C_\delta}{\rho_{soot}} C_\alpha \rho^2 \bar{T}^{1/2} \bar{X}_{CxHy} e^{-T_\alpha/\bar{T}} + \frac{C_\gamma}{\rho_{soot}^{1/3}} \rho \bar{T}^{1/2} \bar{X}_{CxHy} e^{-T_\gamma/\bar{T}} \bar{n}^{1/3} \bar{f}_v^{2/3} \tag{20}$$

where N_0 is the Avogadro's number, and ρ_{soot}, the soot density, given as 1800 kg/m^3. The values of the empirical constants, such as C_α, C_β, C_δ, C_γ, T_α and T_γ, were experimentally determined by Moss et al. [13]. The first term in Eq.(19) represents the rate of particle nucleation and the second the coagulation of soot. The last term in Eq.(20) represents the surface growth of soot which contained a linear dependence on aerosol surface area. The Moss model does not include a term for turbulent soot oxidation due to O_2 which results in lower soot volume fraction in a turbulent diffusion flame. In this work, by assuming soot oxidation rate to be identical to the one of mixing-controlled reaction, τ_{mix}, we have included an additional term for soot oxidation rate, $\dot{\omega}_{Oxid}$, by using an Eddy-Break-Up approach.

$$\dot{\omega}_{Oxid} = \rho\,\tau_{mix}\min\left(1,\ \frac{\rho \bar{Y}_O}{\bar{c}_s \nu_s + \rho \bar{Y}_F \nu_F}\right) \tag{21}$$

Here, c_s denotes the soot concentration which can be derived from the soot number density (Eq.16) and the mass of a soot particle. The symbols, ν_s and ν_F, are the stoichiometric oxygen requirements to burn 1 kg soot and fuel, respectively. This model represents the rationale approach to taking into account the turbulence effects on soot oxidation rate in the case where the respective rates of mixing-controlled reaction are unlikely to be known.

2.4 Radiation Model

The radiation intensity, I, is found by solving the radiative transfer equation without scattering in the domain, Ω, of the radiation propagation.

$$\vec{\nabla}.\vec{\Omega} I + \kappa I = \kappa \frac{\sigma \bar{T}^4}{\pi} \tag{22}$$

Here, σ denotes the Stefan-Boltzmann constant. Eq.(22) includes a balance of radiant energy emitted into the direction of the radiation propagation, $\vec{\Omega}$, and the radiant energy attenuation through the absorption coefficient, κ, in the medium. The overall absorption coefficient, κ, for the soot and gas (CO_2 and H_2O) mixture is calculated from a pseudo grey gas approximation through Modak model [19] in function of the temperature and concentration of combustion products. The divergence of the radiative flux, $-\nabla \cdot q_r$, in the energy equation (5) is calculated from a discrete expression, based on a Finite Volume Method described in Ref. [11] by introducing a weighting factor, w^l, in the direction l.

$$-\nabla \cdot q_r = -\int_{4\pi} \vec{\nabla}.\vec{\Omega} I d\Omega \approx \kappa\left(\sum_{l=1}^{L} w^l I^l - 4\sigma \bar{T}^4\right) \tag{23}$$

For situations where the burning walls are a diffusively reflecting and emitting surface, the radiative boundary condition is given by

$$I(r_w, \Omega) = \frac{\varepsilon_w \sigma T_w^4}{\pi} + \frac{1-\varepsilon_w}{\pi}\int_{n.\Omega} |n.\Omega'| I(r_w, \Omega') d\Omega' \tag{24}$$

where $I(r_w, \Omega)$ is the intensity at the wall, ε_w the wall emissivity, and T_w the wall surface temperature. The Ω' means that only the incoming directions are taken into account when calculating the reflection.

2.5 Method of Resolution

The finite-difference technique is used to discretize the partial differential equations. This procedure entails the subdividing of the calculation domain into a finite number of cells. The velocities are taken on the boundary of each cell; and all the

scalar variables are taken at cell centres. This staggered grid leads to a very efficient differencing scheme for the equations. All spatial derivatives are approximated by second-order central differences and the flow variables are updated using an explicit second-order Runge-Kutta scheme. In FDS [11], the momentum equation is simplified by subtracting off the hydrostatic pressure gradient from the momentum equation, and then dividing by the density. An elliptic partial differential equation can be obtained by taking the divergence of the momentum equations, yielding a Poisson (pressure-like) equation which is solved with a fast, direct method [11]. The inert solid surface is considered as adiabatic, and the no-slip condition is imposed by setting all velocities to zero. The burning surface is considered as a pure combustible material.

3. RESULTS AND DISCUSSION

The predicted flame structures corresponding to a fire between two burning walls and a single wall burning opposed an inert wall in parallel configuration are shown in Fig. 2(a,b). The processes of air entrainment into the gap are clearly evident in Fig. 3, and the velocity vectors are approximately parallel to the burning wall due to buoyant vertical acceleration. The boundary layer flame is essentially confined to the gap between the burning walls. The excess combustible gases which serve as a burner, are ejected out of the gap where they burn on contact with the abundant ambient oxygen. Consequently, past the burning wall, coherent periodic oscillations of the flame (cf. Fig. 2) arising from air entrainment in a cyclic manner due to buoyancy appear with increasing magnitude of the turbulence intensity. The ability of the mathematical models described is first tested against experimental data from an intermediate-scale facility. The schematic diagram of the release examined experimentally [3], and the coordinate system adapted in numerical simulation are shown in Fig. 2. In the experiment, the tests used sintered bronze burners which were mounted on a wall height, H, of 1 m and width, W, of 0.4 m with a separation distance of L = 0.1 m. Although, the wall fire facility is 3D in nature, the reacting flow is essentially 2D in nature. Therefore, the measurements were performed only in the median plane (x-z, y = W/2). The fuel (propane, C_3H_8) supply rate was 3 g/m^{2}s, adjusted to give a Heat Release Rate (HRR) of 52 kW for a single wall, and 104 kW for two walls burning. Temperatures were obtained by means of fine wire thermocouples. Velocity and its fluctuation were determined using a two-component Laser Doppler Velocimetry (LDV) system. For possessing a predictive capability, it is important to understand what length scales must be resolved. In general, the characteristic length scale, L*, is related to the HRR, Q (kW), by the relation [11]

$$L^* = \left(\frac{Q}{\rho_\infty T_\infty c_p \sqrt{g}} \right)^{2/5} \quad \text{(m)} \qquad (25)$$

Here, ρ_∞ is the ambient density, T_∞ the ambient temperature, c_p the specific heat of the gas, and g acceleration of gravity. The large scale structure that is controlled by the inviscid terms can be completely described when this characteristic length L* is spanned by roughly ten computational cells [11].

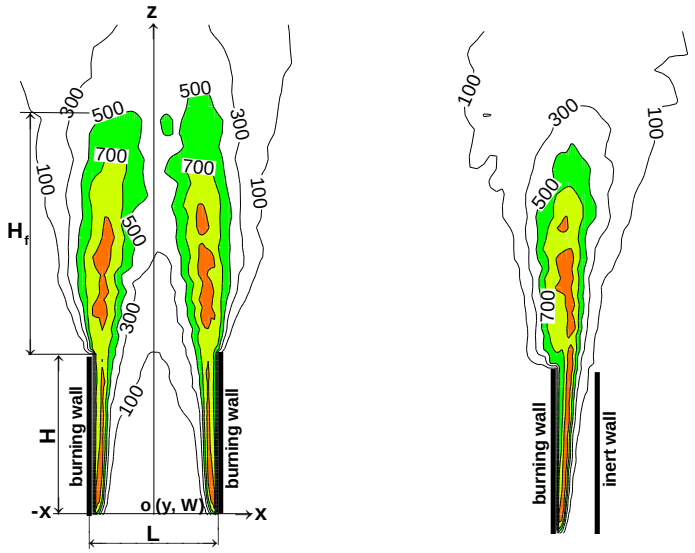

(a) Two walls burning (b) Single wall burning

Fig. 2: Flame structure of the buoyancy-induced fire in parallel vertical panel geometry

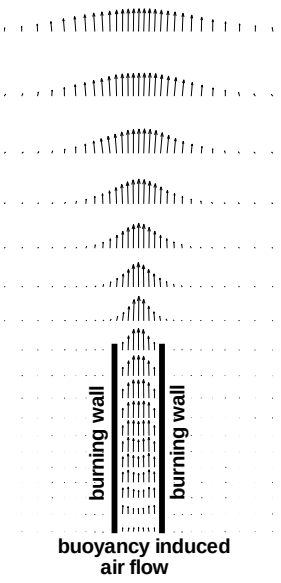

Fig. 3: Velocity vectors of the buoyancy-induced fire between two burning walls in parallel configuration

For the wall fire in parallel configuration (cf. Fig. 2), the characteristic length, L*, is in an order of 0.3 m for a HRR of 52 kW. This implies that adequate resolution of this wall fire in large-scale can be achieved with a spatial resolution of about 0.03 m. Based on this spatial reference value, the extra grid points are added in the burning wall region where a strongly stratified layer is developed. By taking into account the flame propagation past the burning wall, an extended region measured 2 m x 1 m in x-y plane, and 5 m in height (z) should be employed. At first, the calculations were performed using a computational mesh with 120 cells in the direction x, 60 cells across (y) and 100 cells in the vertical direction (z). Along the axis x, start at 0.008 m near the burning wall regions, and stretch to about 0.01 m in the centre region. In the vertical direction, z, cell sizes remain about 0.04 m along the burning wall and stretch to about 0.14 m at the top free boundary. An uniform grid is used with cell size of about 0.016 m in the y direction. In the second case, the number of grids with 150(x) x 75(y) x 120(z) was used for adding the more grid cells near the burning wall region. This grid refinement leads to a highly compressed grid system which gives a minimum ratio between cell sizes in x and y or z directions, of the order of 2 in the first case, and 3 in the second case. Using a DEC Alpha workstation, CPU time is of the order of 4 days for a real 20 s simulation in the first case, and practically doubled in the second case. A rectangular window, needed for the LDV measurements, has to be made on each of the walls. For avoiding the perturbations, only at the height of 0.9 m near the wall fire exit, the temperature and velocity were experimentally determined [3]. An output from LES simulations had flow oscillations. The predicted temperature, velocity and root-mean-square (rms) value of the velocity fluctuations, w', are time-averaged over a range of the computational time as

$$\tilde{\phi} = \sum_{i=1}^{N} \bar{\phi} \Delta t_i / \sum_{i=1}^{N} \Delta t_i \qquad (26)$$

Here $\tilde{\phi}$ denotes the mean value of the general variable, ϕ, Δt_i the time step, and N the total number of the time step. In Figs. 4, 5 and 6, the predicted time-averaged temperature/ velocity and normalized velocity fluctuation, w'/w (w, the local mean velocity), are compared with the measurements. The most significant discrepancy is found in the boundary layer near the burning wall. In Fig. 4, it is found that by using the second grid system, the calculated temperature is somewhat improved near the wall region, and however, much lower in the centre region. It should be noted that in a LES calculation, commutation of the filtering operation with temporal and spatial differentiation is only strictly valid for uniform grid system. The second highly compressed grid system makes the Smagorinsky sub-grid model too dissipative, contributing to the inaccuracies in the numerical simulation. However, adding the more grid cells in the other two directions (y and z) for reducing the ratio between cell sizes results in a large computational overhead, severely restricting its range of applicability to a 3D fire simulation. Besides, the water cooling effect during the experiment for protecting the burning wall is not numerically simulated. In the other hand, the experimental uncertainty lies in the measurement of the temperature by the thermocouples in the boundary layer flow near the burning wall region. It can be concluded that the first moderately stretched grid system offered the best tradeoff between accuracy and cost for the present purpose. In spite of the discrepancy, the magnitude and distribution of buoyancy-controlled diffusion flame in parallel configuration are correctly predicted. The velocity by the side of the inert wall (cf. Fig. 5) is very small, and however, the velocity profiles along the burning wall are very similar to those of two burning walls case (cf. Fig. 4). Corresponding to the underestimation of the maximum temperature, the velocity profile is also underpredicted both with a difference equal to about 10%. The velocity fluctuations (cf. Fig. 6) are overpredicted, the difference is noticeable, particularly for the single burning wall case near the inert wall. The higher value of the normalized velocity fluctuation is maintained over a large region between the parallel walls due to the buoyancy-induced flame instability. Both the experiment and prediction show that the presence of an inert wall enhances the normalized axial

velocity fluctuations due to the weak local mean velocity.

While it is relatively easy task of obtaining experimental data from a free single vertical wall fire [14] for which an inert wall (cf. Fig. 2b) is removed, allowing a detailed comparison between prediction and experiment. Following the analysis of the characteristic length, L*, the calculations were performed using a computational mesh with 120 cells in the direction x, 60 cells across (y) and 100 cells in the vertical direction (z) in an extended region measured 2 m x 1 m in x-y plane, and 5 m in height (z). Profiles of the mean temperature and axial velocity of the buoyancy-induced flow at different heights, z, along the vertical wall, are presented in Figs. 7 and 8. The fire results in an acceleration of the air stream due to the combined effects of natural convection and air entrainment, resulting in an increase of the maximum axial velocity from 1.8 to 2.8 m/s. The predicted axial velocity fluctuation, w'w' are compared with the measurement at the heights of 0.47 and 0.72 m in Fig. 9. A free wall burning includes an almost laminar boundary layer diffusion flame at the low part of the wall (z/H < 0.4), and a turbulent, intermittent one as it evolves upward. The location of the maximum velocity fluctuation is very close to the burning wall, as a consequence of the stronger shear stresses there. Far away from the wall, the higher velocity fluctuation is mainly due to the buoyancy-induced oscillations of the flame. The turbulence level affects the maximum temperature one which decreases from 1260 K at the low part of the wall (x/H < 0.4) to 1080 K in the fully developed turbulent region.

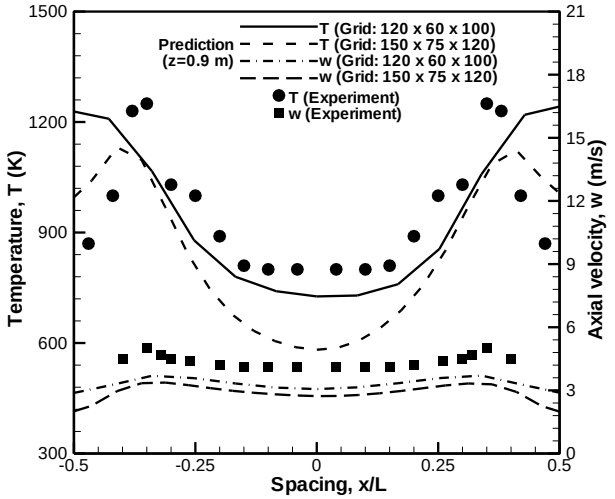

Fig. 4: Comparison between the predicted and measured mean temperature and velocity from a two burning walls fire at the height of 0.9 m

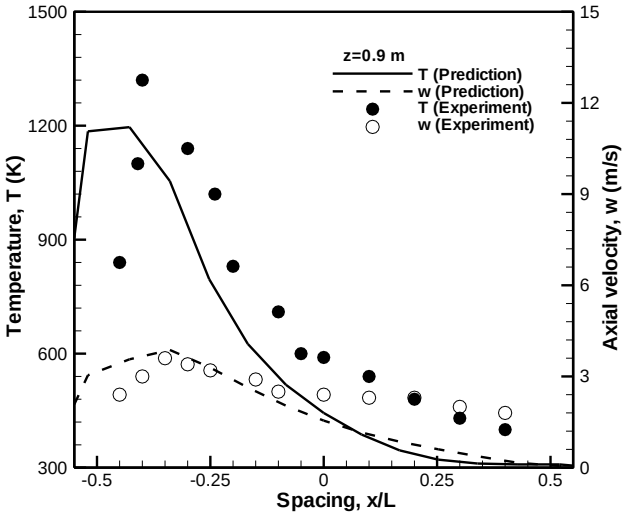

Fig. 5: Comparison between the predicted and measured mean temperature and velocity from a single wall burning in parallel configuration at the height of 0.9 m

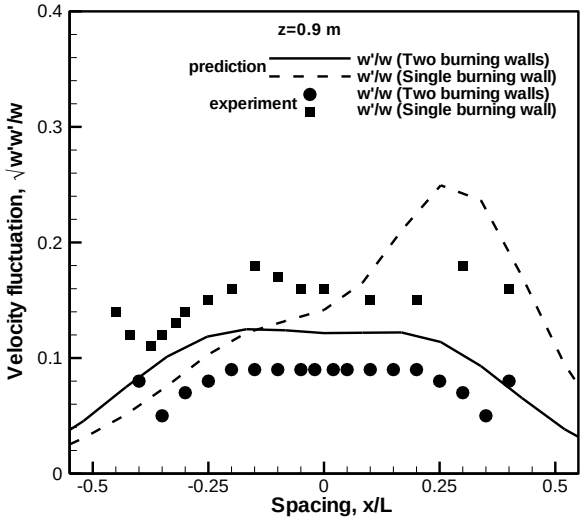

Fig. 6: Comparison between the predicted and measured longitudinal velocity fluctuations from a single and two walls burnings at the height of 0.9 m

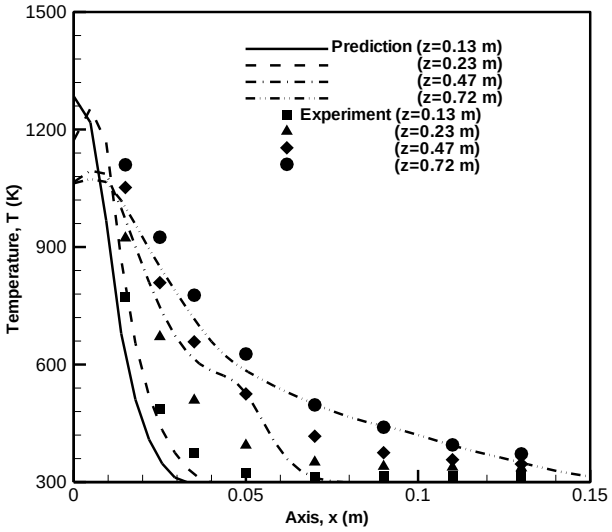

Fig. 7: Comparison between the predicted and measured mean temperature from a free single wall burning at the different heights

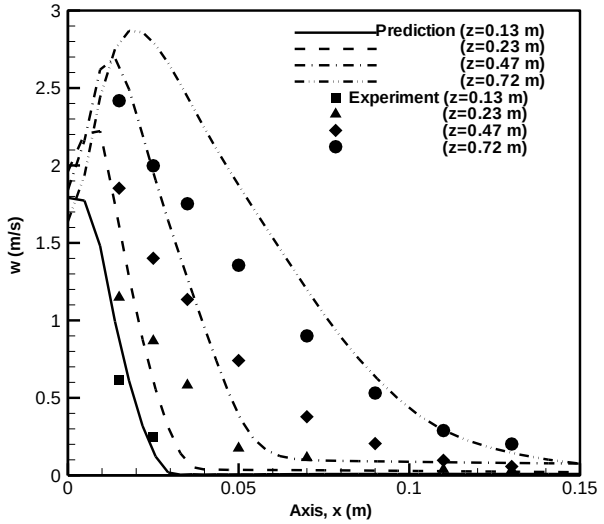

Fig. 8: Comparison between the predicted and measured mean longitudinal velocity from a free single wall burning at the different heights

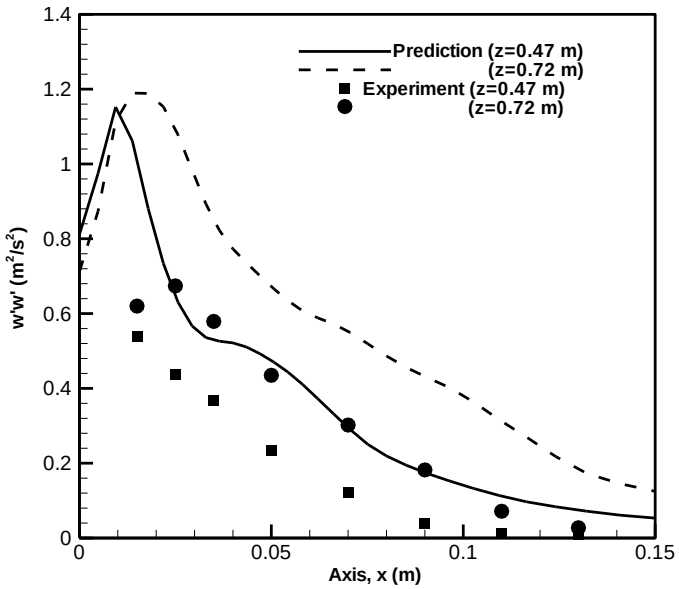

Fig. 9: Comparison between the predicted and measured longitudinal velocity fluctuation from a free single wall burning at two vertical locations

There are still very few experimental data available including CO and soot distributions along the vertical wall fire against which model predictions can be validated and assessed due to the high cost and instrumentation difficulty. By means of the numerical models, effects of the separation distance, by considering a range of the ratio, L/H, between the spacing (L) and height (H) varying from 0.06, 0.1, 0.15, 0.2, 0.25, 0.35 up to 0.45, on CO and soot productions are investigated. The vertical walls are considered as a plastic type condensed fuel with a pyrolysis rate of 20 g/m^{2}s. Two characteristic flame features are identified by varying the ratio, L/H. For the ratio lower than 0.2, the two diffusion flames are initially separated inside the gap, and meet each other due to the progressively increasing magnitude of the flame thickness to merge into a turbulent jet flame. As an illustration, contours of the CO mass fraction (percent) and the soot volume fraction (ppm) in the median plane are presented in Figs. 10 and 11. Abundant CO and soot productions are formed in the oxygen-lean fuel-rich boundary layer since there is not enough oxygen for CO oxidation into CO_2. For a global description along the height of the burning wall, the mean levels of CO and soot production are determined by integrating the local values across the transversal section at a given height z, and then averaging this sum by the corresponding section. Evolutions of the mean levels of the CO mass fraction and the soot volume fraction (ppm) along the height as a function of the ratio, L/H, are depicted in Figs. 12 and 13. Inside the narrowest spacing (L/H = 0.06) between the burning walls, the lowest level of the CO production is formed due to cessation of the chemical reaction caused by reduction in the fresh air entry. An increase of the ratio, L/H, to 0.2 results in the highest level of the CO production inside the gap due to an increase of the air entrainment. Outside the gap (z/H > 1), the narrowest spacing (L/H = 0.06) gives the most pronounced CO production due to the presence of the abundant unburned fuel. Conversely, the soot volume fraction undergoes a rapid increase inside the narrowest spacing (L/H = 0.06) due to presence of the abundant unburned fuel and the higher temperature level (T > 600 °C). The merging of the two diffusion flames inside the narrower spacing (L/H < 0.2) induces the higher values of the soot volume fraction due to lack of the oxygen for soot oxidation. With an increase of the ratio, L/H, to 0.2, the soot volume fraction decreases due to an increase of the air entrainment which enhances the soot oxidation rate. When the ratio, L/H, becomes sufficiently great (L/H >> 0.2), the vertical parallel walls burn separately all along the burning wall, reducing significantly the interaction between the two diffusion flames, and thus, the combustion intensity. Consequently, the level of the maximum soot volume fraction increases near the leading edge region where the diffusion flame becomes essentially laminar, and approaches asymptotically that of a single burning wall. Variation of the ratio, L/H, has also a pronounced impact on the convection flux (cf. Fig. 14) calculated from a wall function [20], and flame-surface radiation flux (cf. Fig. 15) along the wall centreline. During numerical simulation in transient mode, the wall surface temperature increases progressively up to about 200°C, and the heat fluxes correspond to this thermal boundary condition. For the smallest ratio of 0.06, in spite of the high level of the soot volume

fraction, the convection and radiation fluxes are found to increase to a maximum at low part of the burning walls (z/H < 0.3), then a dramatic reduction in both the convection and radiation fluxes is brought about beyond that region due to flame exhaust. An increase of the ratio, L/H, to 0.15 improves significantly the radiation flux which, as a whole, is proportional to both the flame volume and the radiation view factor associated with the ratio, L/H. A further increase of the ratio to 0.2, results in a reduction in radiation flux mainly due to the decreases of both the flames interaction and the soot volume fraction. The separation of the two diffusion flames for the ratio higher than 0.35 results in an increase of the radiation flux at the low part of the burning wall due to the high level of the soot volume fraction (cf. Fig. 13), approaching approximately that of a single burning wall.

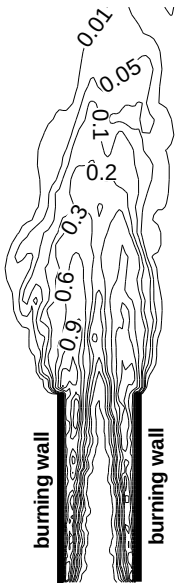

Fig. 10: Iso-contours of the carbon monoxide mass fraction (percent) from the two burning walls in parallel configuration

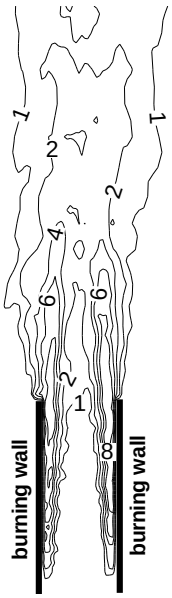

Fig. 11: Iso-contours of the soot volume fraction (ppm) from the two burning walls in parallel configuration

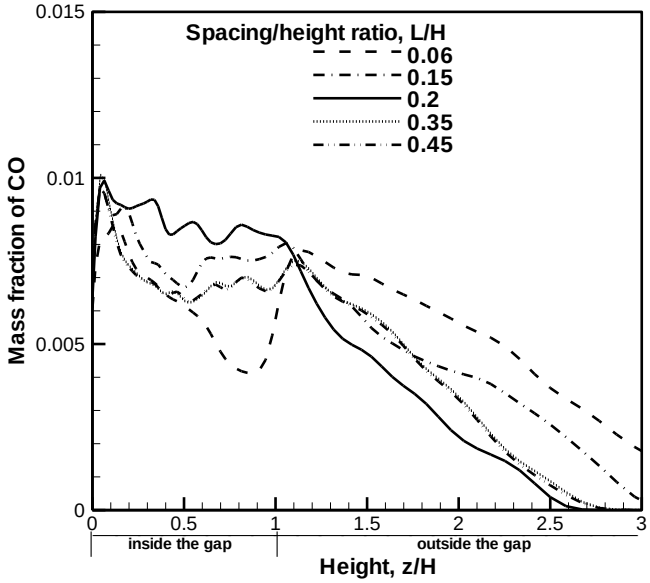

Fig. 12: Evolution of the mean level of carbon monoxide mass fraction along the height for the different ratio, L/H

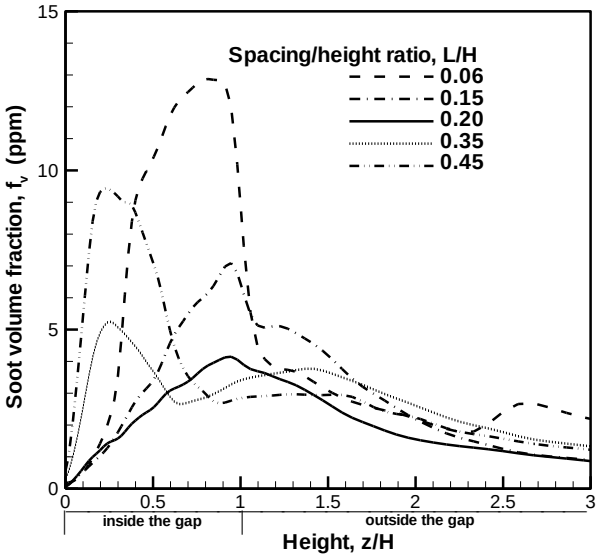

Fig. 13: Evolution of the mean level of soot volume fraction (ppm) along the height for the different ratio, L/H

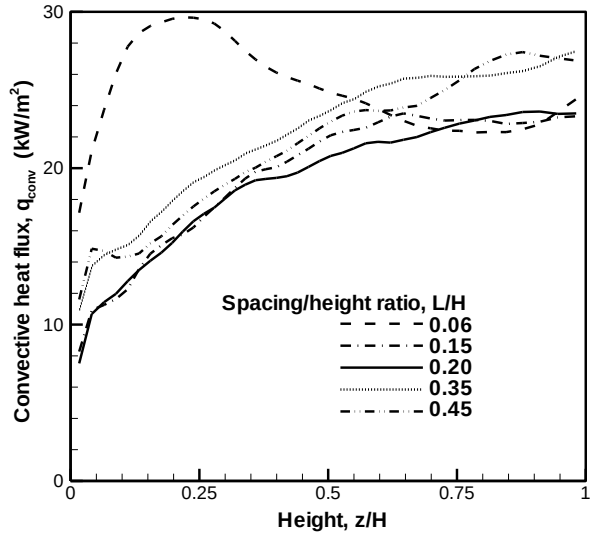

Fig. 14: Evolution of the convection flux along the burning wall for the different ratio, L/H

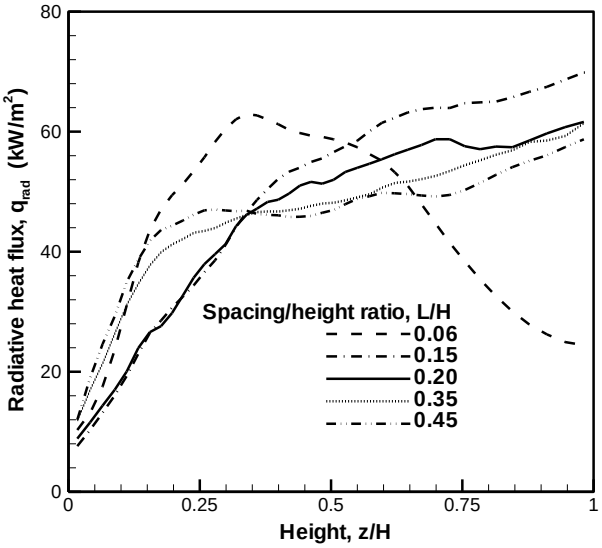

Fig. 15: Evolution of the flame-surface radiation flux along the burning wall for the different ratio, L/H

Different condensed fuel of the vertical walls was simulated by varying the pyrolysis rate, m_F, from 3, 5, 10, 15 up to 20 g/m^{2}s. According to the experiment, for a heavily sooting flame, the visible flame shape corresponds to the zone where the gas temperature is higher than 500°C, and this criterion is used for determining the predicted flame shape. In the case where a merging of the diffusion flames occurs (L/H < 0.2), a critical pyrolysis rate of 10 g/m^{2}s is predicted, beyond which the combustion efficiency, which is determined from the ratio between the calculated and the theoretical heat release rates, enters rapidly the decay phase up to about 60%. Below this critical value, there is an excess of oxygen in the flame zone, and an increase of the pyrolysis rate from 3 to 10 g/m^{2}s induces an increase of the flame height, H_f, from 0.4 to 1.2 m past the burning wall. Conversely, as the pyrolysis rate surpasses the critical value, the oxygen within the gap is insufficient to consume the fuel accumulated inside the gap; the combustion within a vitiated gap is close to rich limit of flammability, and the flame height past the channel, H_f, is approximately two times of the burning walls ($H_f \approx 2H$). Evolution of the mean level of the CO mass fraction and the soot volume fraction (ppm) along the height is depicted in Figs. 16(a,b) and 17(a,b). Near the leading edge region (z/H < 0.3) where an almost laminar diffusion flame is established, the amplitude of the CO production appears remarkable. Far away from that region, the CO production is found to be maintained an almost constant value inside the gap (L/H < 1), because both the mass flux of entrained fresh air and the turbulence development limit the increase of the CO production through the oxidation rate. Once outside the gap, the CO production enters rapidly the decay phase due to enough oxygen and strong flame oscillations, both enhancing the CO oxidation into CO_2. The presence of an inert wall does not affect the level of the maximum CO production, and however, reduces the region of the CO presence past the burning wall. While as a burning wall is replaced by an inert one (cf. Fig. 2b), the axial positions, z/H, of the maximum soot formation shift from 0.4 to 0.9. For the two burning walls (cf. Fig. 17a), the soot volume fraction continues to increase steadily until it attains a maximum near the burning wall exit (z/H = 0.9), and rapidly decreases downstream due to the dilution and the strong turbulent oxidation on contact with the abundant ambient oxygen. However, with the presence of an inert wall (cf. Fig. 17b), the maximum soot volume fraction occurs near the middle of the gap (z/H = 0.4) due to a decrease of the oxidation rate in laminar flame region. Far away from that region (z/H = 0.4), the oxidation rate is enhanced by the turbulence development of the buoyancy-induced flow, reducing later the soot production. The levels of the soot volume fraction and CO production, as a whole, increase for an increase of the pyrolysis rate from 3 up to a critical value of 10 g/m^{2}s, and approach an asymptotical profile beyond the critical value due to the decaying combustion efficiency. The convection flux (cf. Fig. 18) and flame-surface radiation flux (cf. Fig. 19a,b) along the wall centreline are analysed. For the weak pyrolysis rate (< 5 g/m^{2}s), the peak of the convection flux is found to be located near the inlet zone, and a high value (25 kW/m^2) of the convection flux is maintained because the diffusion flame is attached to the burning surface, inducing a pronounced temperature gradient there. An increase of the pyrolysis rate induces a reduction in convection flux mainly due to an increase of the flame stand-off distance which reduces the temperature gradient near the wall. For the two burning walls, an increase of the peak radiation flux (cf. Fig. 19a) from 25 to 60 kW/m^2 is brought about with an increase of the pyrolysis rate from 3 to a critical value of 10 g/m^{2}s due to increase in the HRR. However, the radiation flux approaches an asymptotical value once the pyrolysis rate surpasses this critical value due to the decaying combustion efficiency (60%) which controls the temperature field. The presence of an inert wall (cf. Fig. 19b) instead of an opposing burning wall (cf. Fig. 19a) results in a significant reduction of approximately 40% in the maximum radiation flux. For the parallel vertical wall fire, although radiation flux seems the central and dominant mode of heat transfer, convection flux plays also a significant role (> 30%).

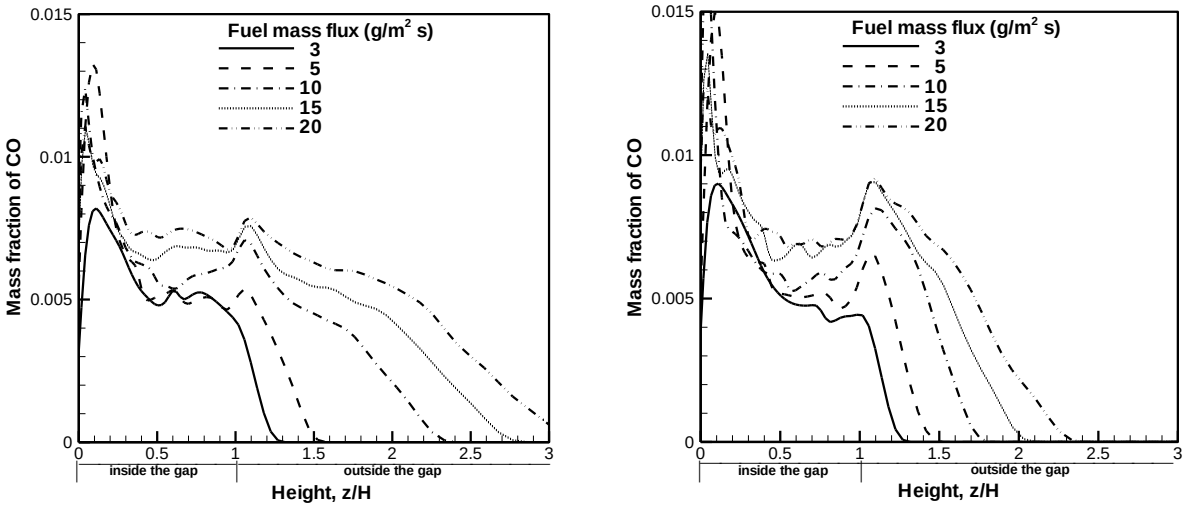

(a) Two walls burning (b) Single wall burning

Fig. 16: Evolution of the mean level of carbon monoxide mass fraction along the height as a function of the pyrolysis rate

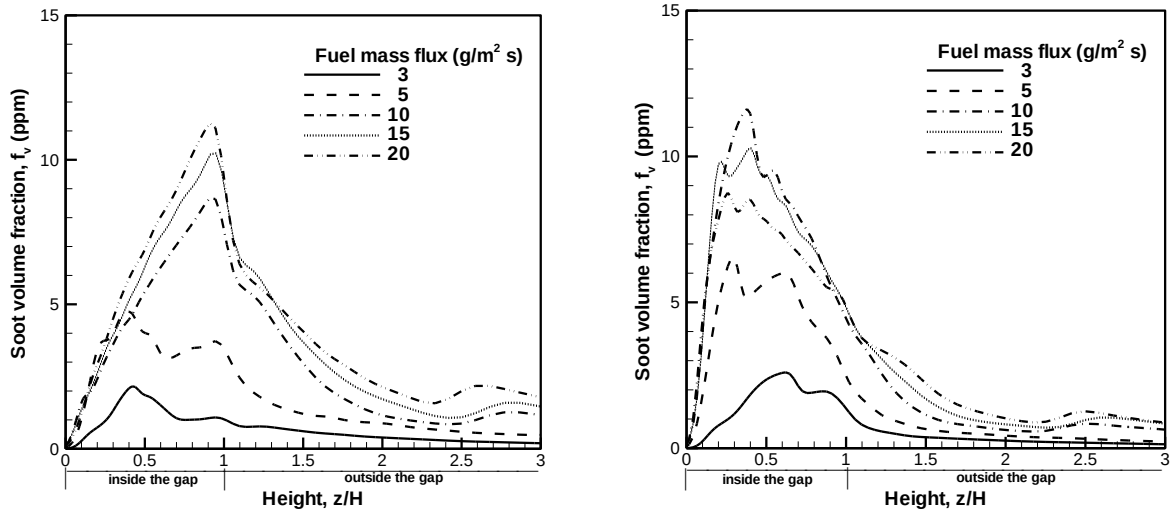

(a) Two walls burning (b) Single wall burning

Fig. 17: Evolution of the mean level of soot volume fraction (ppm) along the height as a function of the pyrolysis rate

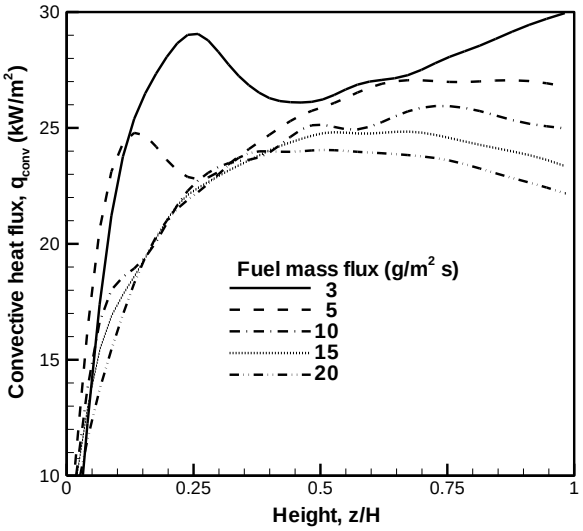

Fig. 18: Convection flux along the burning wall as a function of the pyrolysis rate

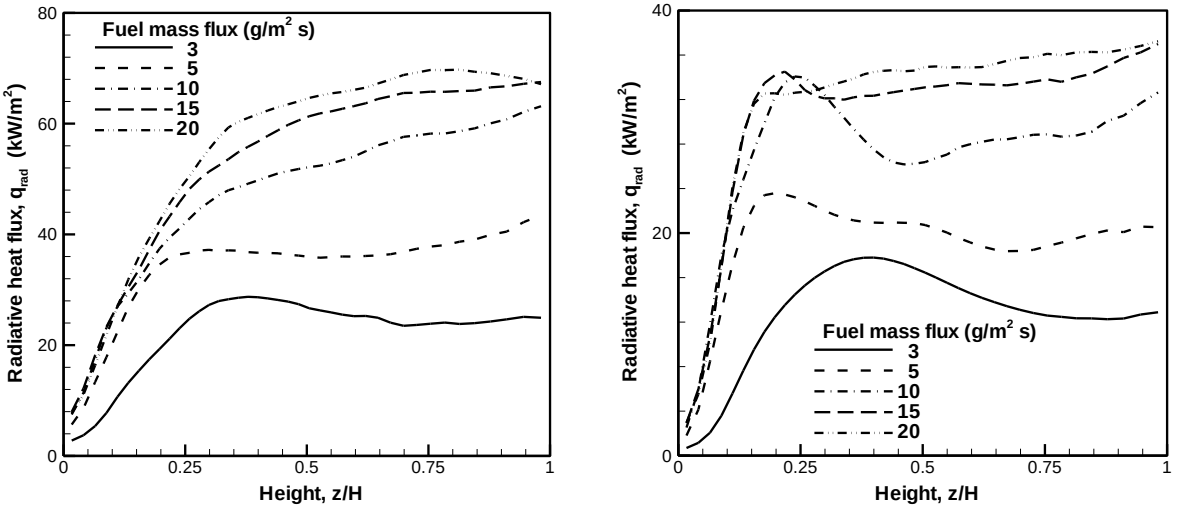

(a) Two walls burning (b) Single wall burning

Fig. 19: Evolution of the flame-surface radiation flux along the burning wall as a function of the pyrolysis rate

4. CONCLUSION

A numerical study of the vertical parallel wall fire with a buoyancy-induced flow is performed by using a Large-Eddy-Simulation. The numerical models are shown to possess the ability to predict the influences of pyrolysis rate and separation distance between the burning walls on soot and CO production. The ratio, L/H, lower than 0.2 generates a merging flame that enhances significantly the soot formation and the associated radiation flux. When the ratio, L/H, becomes sufficiently great (L/H > 0.2), the abundant soot is formed near the leading edge region where a laminar diffusion flame is established. While, the CO production seems less sensitive to the change in the ratio, L/H. In the case where the two diffusion flames merging occurs (L/H < 0.2), a critical pyrolysis rate of 10 g/m^{2}s is predicted, below which the flame height, H_f, past the burning wall increases with the pyrolysis rate. Once the pyrolysis rate surpasses this critical value, the flame height past the burning walls remains approximately constant with $H_f \approx 2H$ due to the decaying combustion efficiency. The maximum soot and CO production approach an asymptotical value as the pyrolysis rate is beyond this critical value. The two opposed burning walls induce an increase of approximately 40% in the maximum radiation flux as compared to a single burning wall.

Further work is underway for a transient fire growth and progressive vitiation of the ambient medium in a parallel panel geometry with self-sustained solid fuel. The turbulent mixing should be improved for accounting for the boundary layer near the burning wall through a dynamic subgrid-scale turbulence model for the future application.

NOMENCLATURE

C_{Ebu}	constant in EBU model
c_p	specific heat of the gas
c_s	soot concentration
C_s	Smagorinsky constant
C_α, C_β, C_δ, C_γ	constants in soot model
C_μ, C_ε	empirical constants in turbulence model
f_c	carbon fraction in fuel
f_v	soot volume fraction
g_i	acceleration of gravity in the co-ordinate directions x, y and z
h	enthalpy
H	height of the burning wall
H_f	visible flame height
H_o	heat-release rate per unit mass of oxygen consumed
I	radiative intensity
I^l	radiative intensity for a single ordinate direction, l
k	turbulent kinetic energy
L	distance between the burning walls
L^*	characteristic length scale of the fire
m_F	fuel supply rate
n	soot number density
p	pressure
Pr_t	turbulent Prandtl number
$\dot{q}_c'''$	heat release rate per unit volume
q_r	radiant energy flux
Q	total heat release rate
S_{CO}	production rate of carbon monoxide
S_{ij}	local large scale rate of strain
Sc_t	turbulent Schmidt number
t	time
T	temperature
T_α, T_γ	energy activation of the soot
T_∞	ambient temperature
u_i, u_j	velocity components in the co-ordinate directions x, y and z
w^l	weighting factor in the discrete ordinates method
W	width of the burning wall
x	streamwise coordinate
x_i, x_j	co-ordinate directions x, y and z
X_i	mole mass fraction of the specie, i
y	cross-stream coordinate
Y_i	mass fraction of the specie, i

Greek Symbols

ε	dissipation rate of the turbulent kinetic energy
ε_w	emissivity of the wall surface
μ_t	turbulent viscosity
ν_1^* , ν_2	stoichiometric coefficients
ν_s	stoichiometric oxygen requirement to burn 1 kg soot
ν_F	stoichiometric oxygen requirement to burn 1 kg fuel
ρ	gas density
ρ_{soot}	soot density
ρ_∞	ambient density
Δ	filter width in LES
σ	Stefan-Boltzmann constant
ϕ	general variable
ϕ'	subgrid-scale component
$\dot{\omega}_{CxHy}$	local reaction rate of fuel
$\dot{\omega}_{CO}$	local reaction rate of carbon monoxide
$\dot{\omega}_{O2}$	oxygen consumption rate
$\dot{\omega}_{Oxid}$	soot oxidation rate
$\dot{\omega}_n$, $\dot{\omega}_{fv}$	soot production rate
Ω	domain of the radiation propagation
$\vec{\Omega}$	direction of the radiation propagation
Ω'	incoming direction of radiation
$\tau_{ij,SGS}$	subgrid scale Reynolds stress tensor
τ_{min}	timescale of the reaction rate
κ	total absorption coefficient

Overbar

-	resolvable-scale component

REFERENCES

1. F. Tamanini, and A.M. Moussa, “Experiments on the turbulent burning of vertical parallel walls”, Combustion Science and Technology, Vol. 23, pp. 143-160 (1980).
2. Y. Kurosaki, A. Ito and M. Chiba, “Downward flame spread along two vertical, parallel sheets of thin combustible solid”, Proceedings of the 17th Symposium (International) on Combustion, pp. 1211-1220 (1978).
3. J.M. Most, B. Bellin, P. Joulain and B. Sztal, “Interaction between two burning vertical walls”, Fire Safety Science - Proceedings of the 2nd International Symposium, International Association for Fire Safety Science, pp. 285-294 (1988).
4. H.Y. Wang and P. Joulain, “Numerical study of the turbulent burning between vertical parallel walls with a fire-induced flow”, Combustion Science and Technology, Vol. 154, pp. 119-161 (2000).

5. M. Foley and D.D. Drysdale, "Heat transfer from flames between vertical parallel walls", Fire Safety Journal, Vol. 24, pp. 53-73 (1995).

6. J.L. De Ris and L. Orloff, "Flame heat transfer between parallel panels inferred from flame volumes", Fire Safety Science - Proceedings of the 8th International Symposium, International Association for Fire Safety Science, pp. 999-1010 (2005).

7. U.O. Koylu and G.M. Faeth, "Carbon monoxide and soot emissions from liquid-fueled buoyant turbulent diffusion flames", Combustion and Flame, Vol. 87, No. 1, pp. 61-76 (1991).

8. S. Leonard, G.W. Mulholland, R. Puri and Santoro, "Generation of CO and smoke during underventilated combustion", Combustion and Flame, Vol. 98, pp. 20-34 (1994).

9. S. Ukleja, M. Delichatsios and Y.P. Lee, "Carbon monoxide and smoke production downstream of a compartment for underventilated fires", Fire Safety Science - Proceedings of the 9th International Symposium, International Association for Fire Safety Science (2008).

10. S.M. Hyde and J.B. Moss, "Field modelling of carbon monoxide production in fires", Proceedings of the 8th International Conference InterFlame, Vol. 2, pp. 951-962 (1999).

11. K.B. McGrattan, P.F. Glenn and E.F. Jason, Fire dynamics simulator – Technical reference guide, NIST Technical Report, National Institute of Standards and Technology, USA (2007).

12. A.A.F. Peters and R. Weber, "Mathematical modelling of a 2.25 MW swirling natural gas flame. Part 1: Eddy break-up concept for turbulent combustion; probability density function approach for nitric oxide formation", Combustion Science and Technology, Vol. 110, pp. 67-101 (1995).

13. J.B. Moss, C.D. Stewart and K.J. Young, "Modelling soot formation and burnout in a high temperature laminar diffusion flame burning under oxygen-enriched conditions", Combustion and Flame, Vol. 101, pp. 491-500 (1995).

14. M.O. Annarumma, J.M. Most and P. Joulain, "On the numerical modeling of buoyancy-dominated turbulent vertical diffusion flames", Combustion and Flame, Vol. 85, pp. 403-415 (1991).

15. H.Y. Wang, P. Joulain and J.M. Most, "On the numerical modeling of buoyancy-dominated turbulent diffusion flames by using large eddy simulation and k-ε turbulence model", Combustion Science and Technology, Vol. 176, pp. 1007-1034 (2004).

16. J. Smagorinsky, "General circulation experiments with the primitive equations I. The basic experiment", Monthly Weather Review, Vol. 91, pp. 99-164 (1963).

17. C. Huggett, "Estimation of the rate of heat release by means of oxygen consumption measurements", Fire and Materials, Vol. 4, pp. 61-85 (1980).

18. Z. Wen, S. Yun, M.J. Thomson and M.F. Lightstone, "Modeling soot formation in turbulent kerosene/air jet diffusion flames", Combustion and Flame, Vol. 135, pp. 323-340 (2003).

19. A.T. Modak, "Radiation from products of combustion", Fire Research, Vol. 1, pp. 339-360 (1979).

20. N. Djilali, I. Gartshore and M. Salcudean, "Calculation of convective heat transfer in recirculating turbulent flow using various near-wall turbulence models", Numerical Heat Transfer, Vol. 16, pp. 189-212 (1989).